Sensors and Materials, Vol. 38, No. 6 (2026) 3441–3456
MYU Tokyo

S & M 4512

3D Numerical Investigations of Gas/liquid Two-phase Flow Characteristics in Underground Stormwater Tunnels

Yongjun Kwon,[1] Jae-Seon Yoon,[2] Woochul Kang,[3] and Hyung-Suk Kim[4*]

[1]Department of Civil and Environment Engineering, Kunsan National University,
Gunsan 54150, Republic of Korea
[2]Rural Research Institute, Korea Rural Community Corporation, Ansan 15634, Republic of Korea
[3]Department of Smart Infrastructure Engineering, Kongju National University, Gongju 31080, Republic of Korea
[4]Department of Civil Engineering, Kunsan National University, Gunsan 54150, Republic of Korea

(Received November 24, 2025; accepted June 4, 2026)

Keywords: slug, two-phase flow, 3D numerical analysis, OpenFOAM

In this study, we simulated slug flow using interFoam in OpenFOAM, which enables 3D two-phase flow analysis, and examined flow characteristics such as velocity and turbulent kinetic energy (*TKE*). Numerical simulations were conducted under a total of 12 superficial Reynolds number conditions. The simulations reproduced the phenomenon in which the elongated bubble region behind the liquid slug formed in a narrower and longer shape than that at the front, confirming that qualitative reproduction was feasible. As Re_{SL} increased, slug length decreased and the number of slugs within the pipe increased. Under the $Re_{SG} = 1377$ condition, the velocity ratio U/U_m inside the liquid slug was below 1.2, whereas $U/U_m \geq 1.5$–2.0 appeared in the elongated bubble region. Under $Re_{SG} = 4320$, the elongated bubble region exhibited $U/U_m \geq 2.0$, while the liquid slug showed a relatively low velocity ratio of approximately $U/U_m \approx 1.0$. TKE/U_d^2 was highest primarily along the liquid–gas interface. Under the $Re_{SG} = 1377$ condition, the liquid slug interior showed low $TKE/U_d^2 < 0.05$, whereas values exceeding 2 occurred at the liquid–gas interface. For $Re_{SG} = 4320$, $TKE/U_d^2 = 0.15$–0.3 or higher appeared at the elongated bubble region, while the liquid slug interior showed $TKE/U_d^2 \approx 0.01$–0.1. For V_L/V, under $Re_{SG} = 1377$, the value increased with Re_{SL}, and the temporal fluctuation between the maximum and minimum values was large. Under $Re_{SG} = 4320$, V_L/V also increased with Re_{SL}, but the fluctuation was not pronounced. These results indicate that a three-dimensional numerical model for two-phase flow can reasonably reproduce the complex behavior and flow characteristics of slug flow. From these findings, future work involving the correlation analysis of numerical data and drone-based imaging data may contribute to identifying crack formation mechanisms in underground stormwater tunnels.

1. Introduction

Under recent global climate changes, intense, short-duration rainfall events are becoming increasingly frequent, with greater irregularity and variability than historical patterns. In urban

---

[*]Corresponding author: e-mail: hskim0824@kunsan.ac.kr
https://doi.org/10.18494/SAM6199

ISSN 0914-4935

areas, the expansion of impermeable surfaces such as roads, sidewalks, and roofs often causes rainwater to be rapidly discharged, exceeding the capacity of existing drainage infrastructure. This situation can simultaneously lead to multiple issues, including damage to underground facilities, the deterioration of water quality, and urban flooding. Underground stormwater tunnels play a central role in reducing urban flooding. Surface runoff is collected through existing pipes and conveyed to the tunnel inlet, and descends through vertical shafts to reach the main tunnel located several tens of meters underground, where it is temporarily stored. Initially, the flow behaves as an open channel with a free surface, but it may gradually transition into pressurized pipe flow. During this process, two-phase flow occurs, with liquid and gas moving simultaneously. This can give rise to complex phenomena such as air pocket formation, rapid pressure fluctuations, and sudden air release. These flow characteristics may adversely affect the structural stability of the tunnels and, in severe cases, result in vibration, leakage, or structural failure. Therefore, understanding these two-phase flow characteristics is important, as they can be linked with sensor-based monitoring techniques, such as drone-based imaging, to identify crack formation mechanisms through fluid dynamic correlation analysis, thereby supporting the selection of appropriate concrete materials for improving structural durability.

When liquid and gas flow simultaneously within a tunnel, slug flow can develop under certain velocity conditions, characterized by repeated liquid slugs followed by elongated gas bubbles (Fig. 1). As slugs move, they may capture the leading liquid, growing in size or maintaining a relatively constant length while moving, and small bubbles may be entrained within the liquid. This type of flow is unsteady and irregular. It has various characteristics, such as slug length, translational velocity, the length and distribution of trailing elongated bubbles, and the entrainment or release of small bubbles within the liquid.(1–4) Current urban flood research in South Korea has primarily relied on one-phase, one-dimensional models (e.g., Storm water management model). However, such approaches were limited in their ability to accurately reproduce the complex physical behavior of two-phase flow.(5) One- and two-dimensional numerical analyses of slug flow were unable to fully capture the formation and transitional behavior of three-dimensional slug flows occurring in real systems.(6–8) While three-dimensional numerical simulations using methods such as very-large eddy simulation (V-LES) and multi-fluid volume of fluid (VOF) could provide more detailed analyses, they required highly refined meshes and were computationally expensive.(9–12) Most existing numerical studies of slug flow focused on the formation, translation, and development of slugs, as well as the qualitative reproduction of overall flow patterns. Studies analyzing individual flow components such as

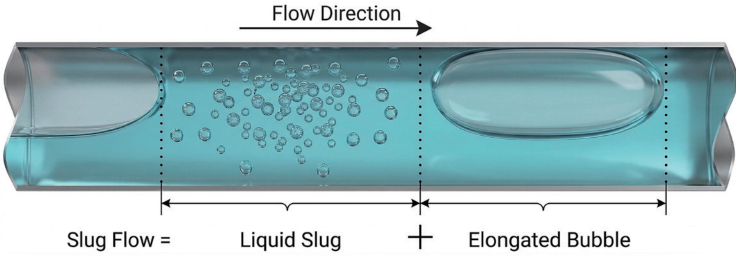

Fig. 1. (Color online) Schematic diagram of slug flow with elongated bubble and liquid slug.

velocity distribution and turbulent kinetic energy (*TKE*) have been conducted to a limited extent. Furthermore, in the field of hydraulic engineering in South Korea, three-dimensional numerical investigations of slug flow were rare, resulting in a lack of reliable foundations to predict unsteady two-phase flow behavior in large-scale underground drainage facilities and to incorporate such behavior into design.

In this study, three-dimensional numerical simulations of liquid–gas two-phase flow are conducted in a horizontal pipe using OpenFOAM to investigate the formation and development of slug flow. The slug flow patterns under different superficial Reynolds number conditions are examined, and the applicability of the numerical model to reproduce slug flow is evaluated through the analyses of velocity distributions, *TKE*, and the rate of liquid volume.

2. Numerical Model

2.1 Governing equations

The three-dimensional two-phase flow was simulated using the OpenFOAM toolbox.(13) The interFoam solver, which is based on the VOF method, was employed to capture the free surface. The governing continuity and momentum equations, expressed using the Einstein notation, are

$$\frac{\partial \overline{u}_i}{\partial x_i} = 0, \tag{1}$$

$$\rho \frac{\partial \overline{u}_i}{\partial t} + \rho \overline{u}_i \frac{\partial \overline{u}_i}{\partial x_j} = -\frac{\partial \overline{P}}{\partial x_j} + \frac{\partial}{\partial x_j}\left[\left(\mu + \mu_t\right)\left(\frac{\partial \overline{u}_i}{\partial x_j} + \frac{\partial \overline{u}_j}{\partial x_i}\right)\right] + \rho g_j + \sigma \kappa \frac{\partial \alpha}{\partial x_i}, \tag{2}$$

where u_i is velocity, t is time, $\overline{P}$ is pressure, ρ is density, μ is viscosity coefficient, μ_t is turbulent viscosity, g_j is gravity acceleration, σ is surface tension, κ is mean curvature, and α is volume fraction. The scalar transport equation for the volume fraction α is solved to capture the free surface interface. The fluid properties are then determined by this volume fraction, as shown in Eqs. (3) and (4).

$$\rho = \alpha \rho_l + \left(1 - \alpha\right) \rho_g \tag{3}$$

$$\mu = \alpha \mu_l + \left(1 - \alpha\right) \mu_g \tag{4}$$

Here, ρ_l, ρ_g are the densities and μ_l, μ_g are the viscosity coefficients of liquid and gas, respectively. $\alpha = 0$ indicates the gas phase, while $\alpha = 1$ indicates the liquid phase. The artificial compression term in the volume fraction transport equation suppresses numerical diffusion, which allows the interfaces between the two fluids to remain sharp. The governing equation for α is expressed as(14)

$$\frac{\partial \alpha}{\partial t} + \frac{\partial(\alpha u)}{\partial x_i} + \frac{\partial\left(\alpha(1-\alpha)u_r\right)}{\partial x_j} = 0, \tag{5}$$

where the final term is the artificial compression term and u_r is the artificial compression velocity, a value based on the maximum velocity field that only affects the free surface interface.

2.2 Numerical methods

OpenFOAM provides various turbulence models, including k-ε, k-ω, and LES models. The finite volume method was adopted as the fundamental framework for the numerical analysis. Different discretization schemes were applied to the governing equations based on the specific characteristics of each term. For the advection term of the momentum equation, a second-order central differencing scheme combined with a limiter was employed. This approach maintains second-order accuracy while simultaneously mitigating potential numerical instability. The advection terms for the turbulence transport equations were discretized using a first-order upwind scheme. Separately, the van Leer TVD scheme was utilized for the VOF equation. The PIMPLE algorithm was used for pressure-velocity coupling. This algorithm, a hybrid of the PISO and SIMPLE methods, is particularly useful for unstable calculations where the Courant number may rapidly increase.

3. Simulation Setup

3.1 Model validation

A model validation was performed by comparing simulation results with the hydraulic experiment data.(15) The benchmark experiment was conducted in a rectangular channel (X = 5.0 m, Y = 0.075 m, and Z = 0.15 m) (Fig. 2). Four turbulence models were evaluated, which are three k-ε (standard, re-normalization group (RNG), and realizable) and k-ω SST models. The computational mesh consisted of 3.15 million cells (1400 × 30 × 75 in X, Y, Z). The inlet boundary conditions were set to a superficial liquid velocity of 0.10 m/s and a superficial gas velocity of 2.50 m/s. Liquid was introduced in the lower 0.215Z of the inlet height, while gas was

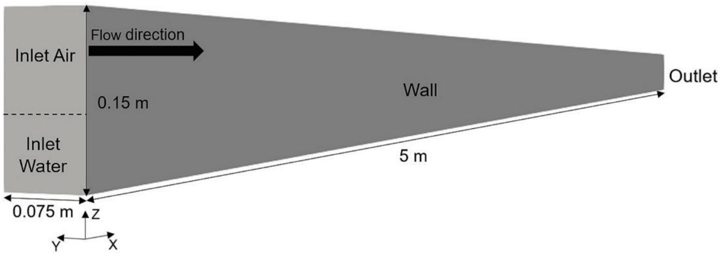

Fig. 2. (Color online) Simulation domain and boundary for model validation.

introduced in the remaining upper region. The results were extracted at X = 2.83 m and Y = 0.0375 m for comparison with the experimental data. As shown in the velocity profile comparison (Fig. 3), the numerical results for both liquid and gas velocities were in good agreement with the measured data near the channel bottom and top. However, a slight tendency to underestimate the velocity was observed near the liquid–gas interface. Despite this minor discrepancy, the models were deemed to accurately predict the overall two-phase flow behavior. Notably, the RNG k-ε model demonstrated the highest overall reproducibility. Previous numerical studies on complex two-phase slug flows have employed various turbulence models depending on a variety of their flow conditions.(9–10,16) Consequently, the RNG k-ε model, which demonstrated the highest quantitative agreement in the model validation with experimental data, was adopted for all subsequent analyses.

3.2 Numerical conditions

The 3D computational domain consisted of a circular pipe with a diameter (D) of 0.025 m and a length (x) of 8 m. This domain was discretized using 2.15 million cells, with grid sizes ranging from 1.7 to 3.0 mm, determined by referencing the grid sizes considered in a previous study.(17) The boundary conditions were defined as follows. At the inlet, a fixed value condition was applied, with the liquid velocity specified for the lower half (0.5D) and the gas velocity for the upper half (0.5D). A no-slip condition was applied to the pipe walls. At the outlet, a zero gradient condition was implemented. A schematic of this computational setup and its boundary configuration is presented in Fig. 4. The total simulation duration was 20 s for each case. This duration was sufficient to allow for the development of slug flow and its propagation along the

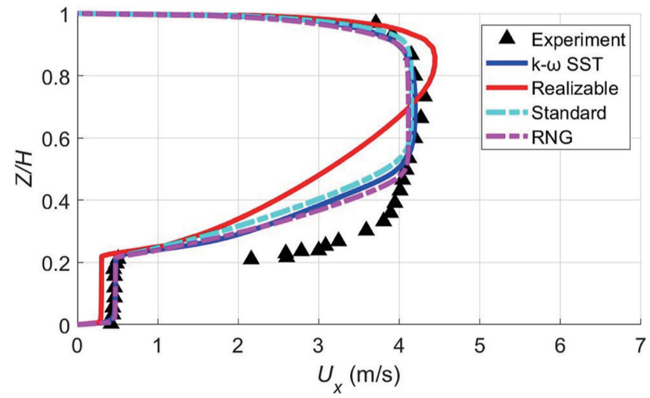

Fig. 3. (Color online) Validation of velocity profiles against experimental data.(15)

Fig. 4. (Color online) Simulation domain for the circular pipe.

entire pipe length. The time step was set in the range of 10^{-5}–10^{-4} s to ensure that the Courant number remained approximately 1.0. While the present 3D model configuration was sufficient to capture macroscopic flow features such as slug formation and translation, the current grid resolution is unable to accurately resolve bubbles smaller than the grid size, which remains a numerical limitation of this study.

A total of 12 simulation cases were performed to analyze various flow patterns. The specific superficial liquid (Re_{SL}) and gas (Re_{SG}) Reynolds number conditions for each case are presented in Table 1. The 12 conditions were selected to correspond with the slug flow regimes illustrated in Fig. 5, following the flow pattern map established by Thaker and Banerjee.(18) These patterns are broadly divided into stratified flow, wavy flow, slug formation, high or less aerated slug flow, and plug flow. The plug flow is specifically defined as a flow type where the liquid slug

Table 1
Details of simulation cases.

Cases	Re_{SL}	Re_{SG}	Flow pattern
Case 1	1420	3540	Slug formation
Case 2	16500	765	Plug flow
Case 3	16500	4000	High aerated slug
Case 4	6500	1377	Less aerated slug
Case 5	7070	1377	Less aerated slug
Case 6	9200	1377	Slug and plug
Case 7	12730	1377	Plug flow
Case 8	16324	1377	Plug flow
Case 9	2830	4320	Slug formation
Case 10	7070	4320	High aerated slug
Case 11	12730	4320	High aerated slug
Case 12	16500	4320	High aerated slug

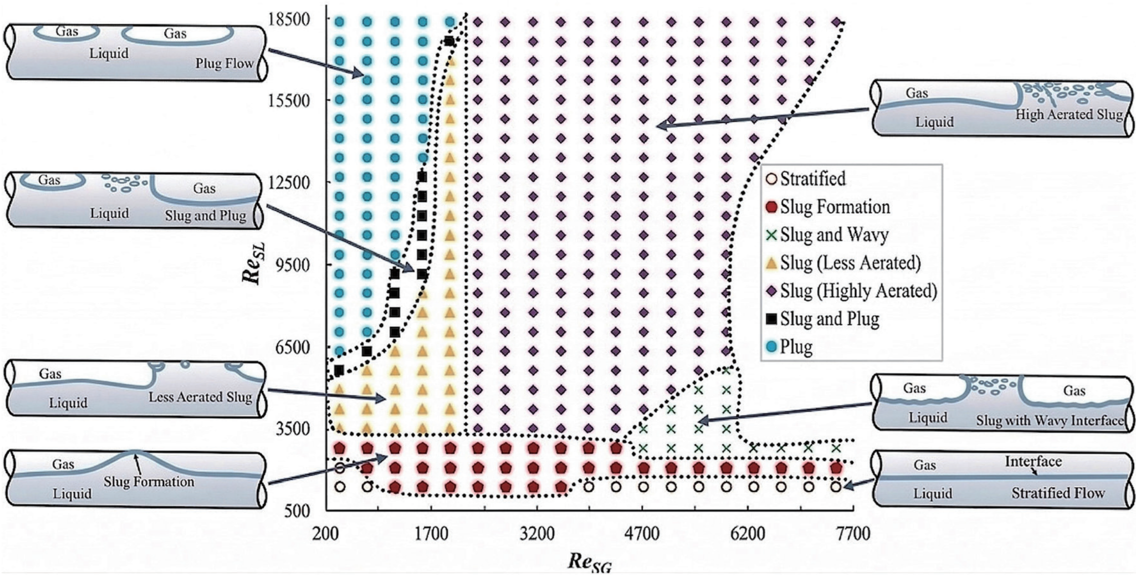

Fig. 5. (Color online) Flow regime map established by Thaker and Banerjee.(18)

moves with very few or no entrained gas bubbles.[19–21] To ensure these conditions would reliably generate slug flow, they were cross-referenced with the onset of slug threshold map shown in Fig. 6. The threshold lines in this map, which have been validated by both Kelvin–Helmholtz (KH) theory and various experiments,[22,23] represent the minimum velocity conditions required for slugging. All 12 cases from Table 1 are located above this minimum threshold, confirming their suitability for this study.

4. Results

4.1 Slug flow analysis

Figure 7 shows the volume fraction results in the x = 3.5–4.5 m section under different superficial Reynolds number conditions. The volume fraction α was defined such that $\alpha = 1$ represents liquid and $\alpha = 0$ represents gas. Figures 7(a)–7(e) show the results under the Re_{SG} = 1377 condition, whereas Figs. 7(f)–7(i) show the results under the Re_{SG} = 4320 condition. At Re_{SG} = 1377, Fig. 7(a), when Re_{SL} = 6500, exhibits a long liquid slug propagating, which is characterized by multiple small air pockets trapped at the top of the pipe. Figure 7(b), where Re_{SL} = 7070, shows that air entrainment begins at the liquid slug front, introducing small bubbles into the liquid slug. Concurrently, the number of air pockets at the top is reduced and the liquid slug length is diminished. In Figs. 7(c)–7(d), at Re_{SL} = 9200 and 12730, respectively, the number of bubbles within the liquid slug progressively decreases. In Fig. 7(e), at Re_{SL} = 16324, the liquid slug length is further reduced. At the higher superficial gas Reynolds number of Re_{SG} = 4320, Fig. 7(f) shows that at Re_{SL} = 2830, the liquid slug contains a large number of small, entrained

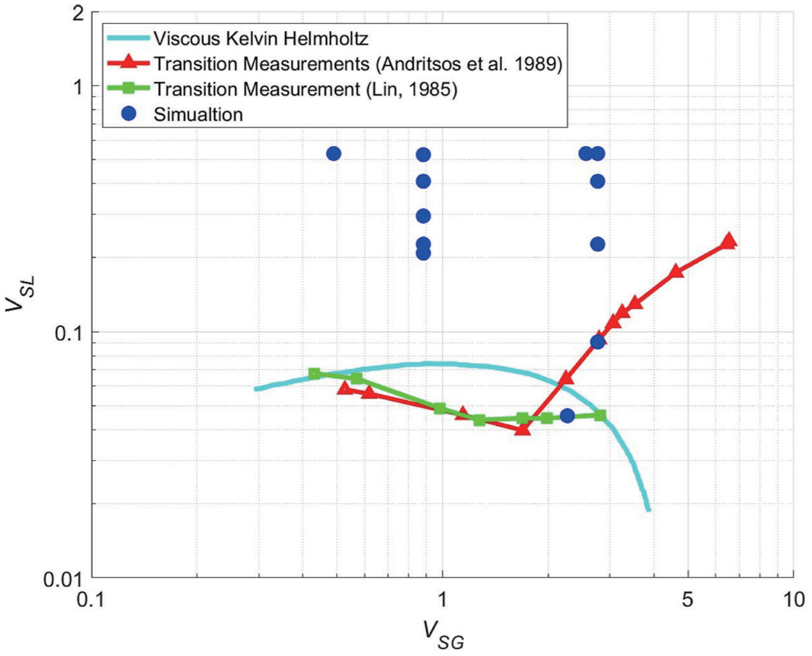

Fig. 6. (Color online) Conditions for onset of slug.

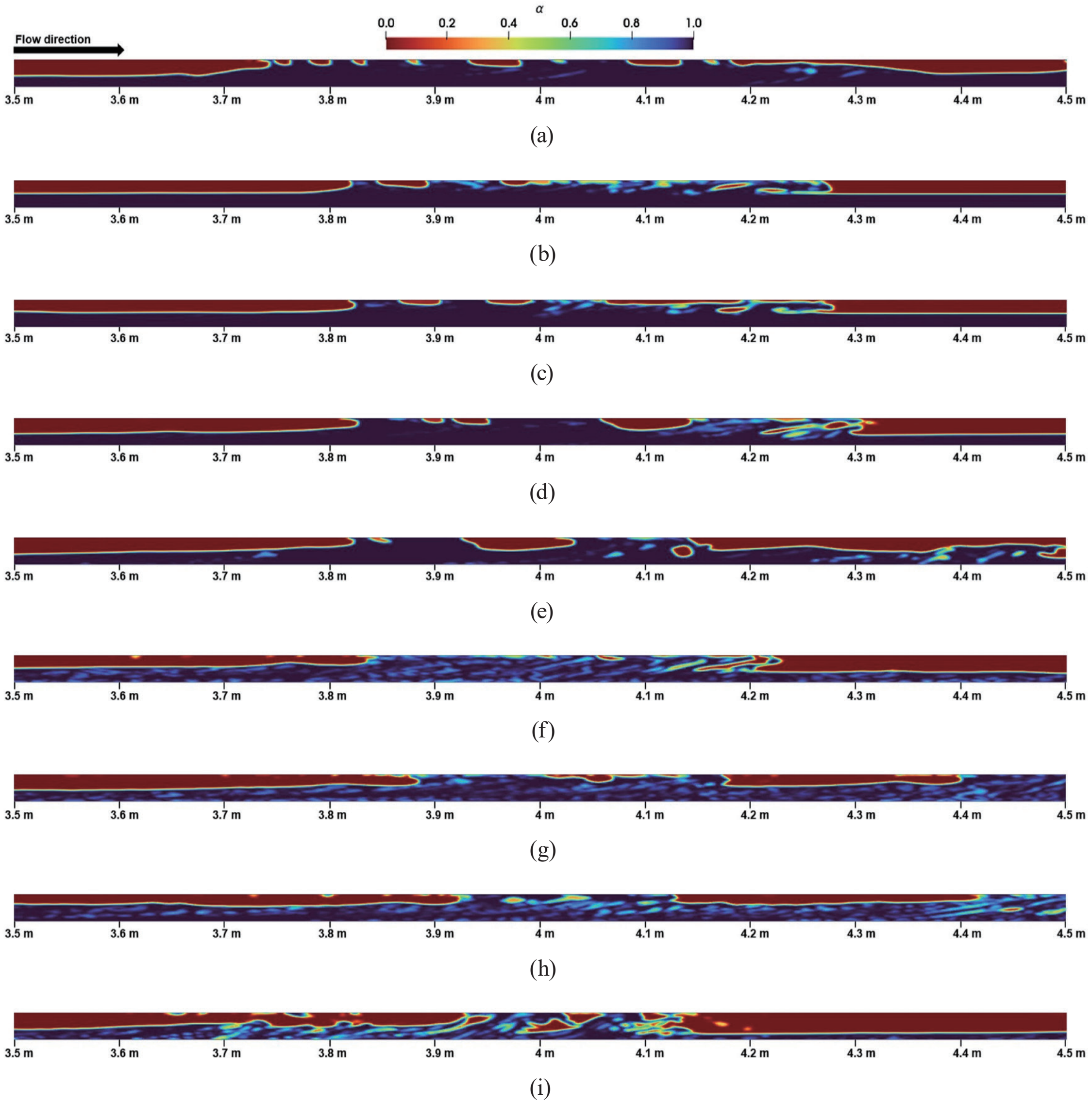

Fig. 7. (Color online) Volume fraction contours at the center cross section. For Re_{SG} = 1377, Re_{SL} = 6500–16324: (a) Case 4, (b) Case 5, (c) Case 6, (d) Case 7, and (e) Case 8. For Re_{SG} = 4320, Re_{SL} = 2830–16500: (f) Case 9, (g) Case 10, (h) Case 11, and (i) Case 12.

bubbles. Notably, detachment initiates at the rear of the slug body, generating small droplets. Figures 7(g)–7(h) show that at Re_{SL} = 7070 and 12730, the slug length progressively decreases, while the entrained bubble concentration within the liquid slug increases. The liquid droplets at the rear also become larger and more numerous. In Fig. 7(i), at Re_{SL} = 16500, the flow develops into a more complex liquid–gas interaction, and distinct, fully developed liquid slugs were not yet established. As a result of the numerical simulation, the rear portion of the elongated bubble is observed to be narrower and longer than its front portion, which is consistent with the phenomenon described by the hydraulic experiment result.(24) Under the Re_{SG} = 1377 condition, an increase in Re_{SL} leads to smaller slug lengths and an increased number of slugs. This occurs because the higher liquid inertia promotes interfacial instabilities (KH), which in turn accelerates the frequency of slug formation. In contrast, the behavior differs at the higher gas velocity of Re_{SG} = 4320. The complex interactions of liquid and gas, induced by the high gas velocity, significantly enhance gas aeration into the liquid slug. This corresponds to the high aerated slug regime classified using Fig. 5, characterized by slugs saturated with gas bubbles and active liquid droplet entrainment at the slug tail. On the basis of these results, the 3D model of this study is evaluated as capable of qualitatively reproducing two-phase slug flow.

4.2 Velocity fields

Figure 8 shows the velocity field results at the center cross section based on superficial Reynolds numbers, where the velocity (U) was normalized by the mixture velocity ($U_m = U_L + U_G$). Figures 8(a)–8(e) present the results obtained under the constant condition of Re_{SG} = 1377, whereas Figs. 8(f)–8(i) correspond to the case of Re_{SG} = 4320. In Fig. 8(a), at Re_{SL} = 6500, a high velocity ratio of $U/U_m \geq 1.5$ is observed in the elongated bubble region, while a relatively low velocity ratio of $U/U_m \approx 1.2$ is observed inside the liquid slug. In Fig. 8(b), at Re_{SL} = 7,070, the elongated bubble region at the top begins to exhibit a high velocity ratio of $U/U_m \geq 2.0$, while the liquid near the pipe bottom at the slug front forms a relatively low velocity ratio of $U/U_m \leq 0.5$. In Fig. 8(c), at Re_{SL} = 9200, high velocity ratios appear in the long air pocket region formed inside the liquid slug, whereas the velocities of small air pockets remain similar to those of the liquid slug. Figure 8(d) shows that at Re_{SL} = 12730, in the elongated bubble region behind the liquid slug, the velocity ratio is relatively low, but still forms $U/U_m \geq 1.5$. In addition, the growth of air pockets inside the liquid slug causes the high-velocity-rate region to expand. In Fig. 8(e), when Re_{SL} = 16324, the elongated bubble region behind the slug exhibits $U/U_m \geq 1.5$, and the velocity in large air pockets inside the liquid slug also reaches $U/U_m \geq 1.5$, whereas small air pockets remain similar to the liquid slug velocity. Figure 8(f) shows that, with an increase in Re_{SG} to 4320, with Re_{SL} = 2830, relatively high velocity ratios are observed in the elongated bubble region both at the front and rear of the liquid slug. In particular, high velocity ratios of $U/U_m \geq 2.0$ appear at the slug rear, and liquid droplets left behind by the moving slug are observed to disturb the flow in the elongated bubble region. In Fig. 8(g), when Re_{SL} increased to 7,070, the elongated bubble region behind the slug experiences a strong disturbance owing to the presence of more liquid droplets, and the velocity ratio in the small air pocket at the top of the liquid slug is around $U/U_m \approx 1.5$. In Fig. 8(h), at Re_{SL} = 12730, the elongated bubble regions at the slug front and rear exhibit high values of $U/U_m \geq 2.0$ over a wider range. Figure 8(i) shows that at Re_{SL} = 16500, $U/U_m \geq 1.5$ appears at the top of the slug, and high velocity ratios of $U/U_m \geq 2.0$ are observed in the elongated bubble region behind the slug and immediately ahead of the slug. Overall, in the elongated bubble region, high velocities of $U/U_m \geq 1.5$–2.0 are predominantly observed near the pipe crown, while the liquid regions inside the slug show relatively lower velocities, slightly exceeding $U/U_m \approx 1.0$. The velocity difference between the slow-moving liquid slug, which occupies the full pipe cross section, and the faster surrounding gas produces strong shear layers at both the front and rear of the slug. Depending on the flow conditions, these shear layers induce gas entrainment into the front of the liquid slug and, under sufficiently high

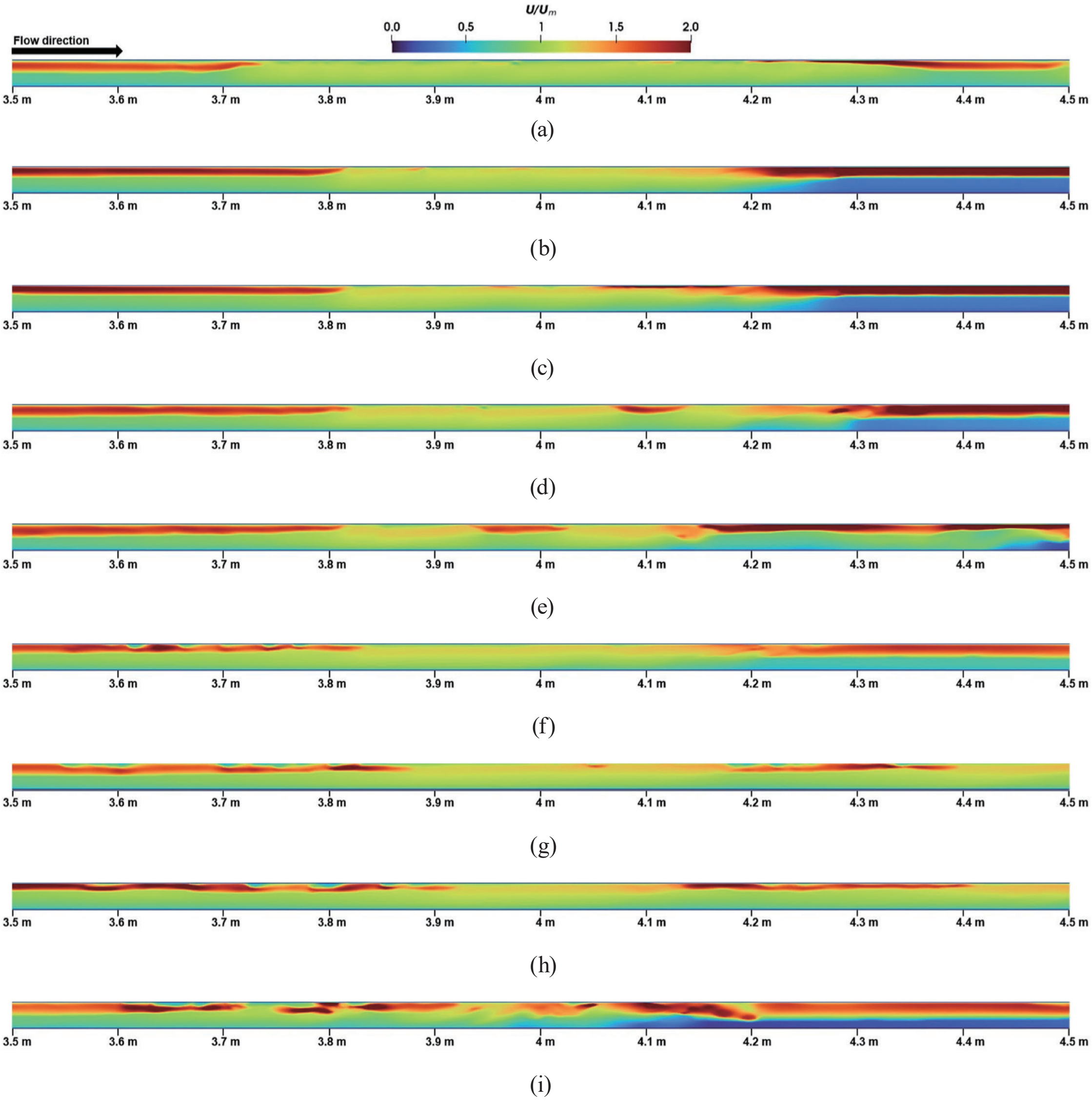

Fig. 8. (Color online) Velocity contours at the center cross section. For $Re_{SG} = 1377$, $Re_{SL} = 6500{-}16324$: (a) Case 4, (b) Case 5, (c) Case 6, (d) Case 7, and (e) Case 8. For $Re_{SG} = 4320$, $Re_{SL} = 2830{-}16500$: (f) Case 9, (g) Case 10, (h) Case 11, and (i) Case 12.

gas velocities, promote droplet shedding from the rear.(25) Together, the gas entrainment and droplet shedding constitute dominant mechanisms controlling slug development and play a critical role in determining the mean slug length and its stability.

4.3 *TKE*

Figure 9 presents the results of *TKE* at the center cross section based on superficial Reynolds numbers. The *TKE* values are normalized by $U_d^2 = (U_L - U_G)^2$. As illustrated in Fig. 9(a), when $Re_{SL} = 6500$, under the constant condition of $Re_{SG} = 1377$, TKE/U_d^2 values exceeding 0.3 are

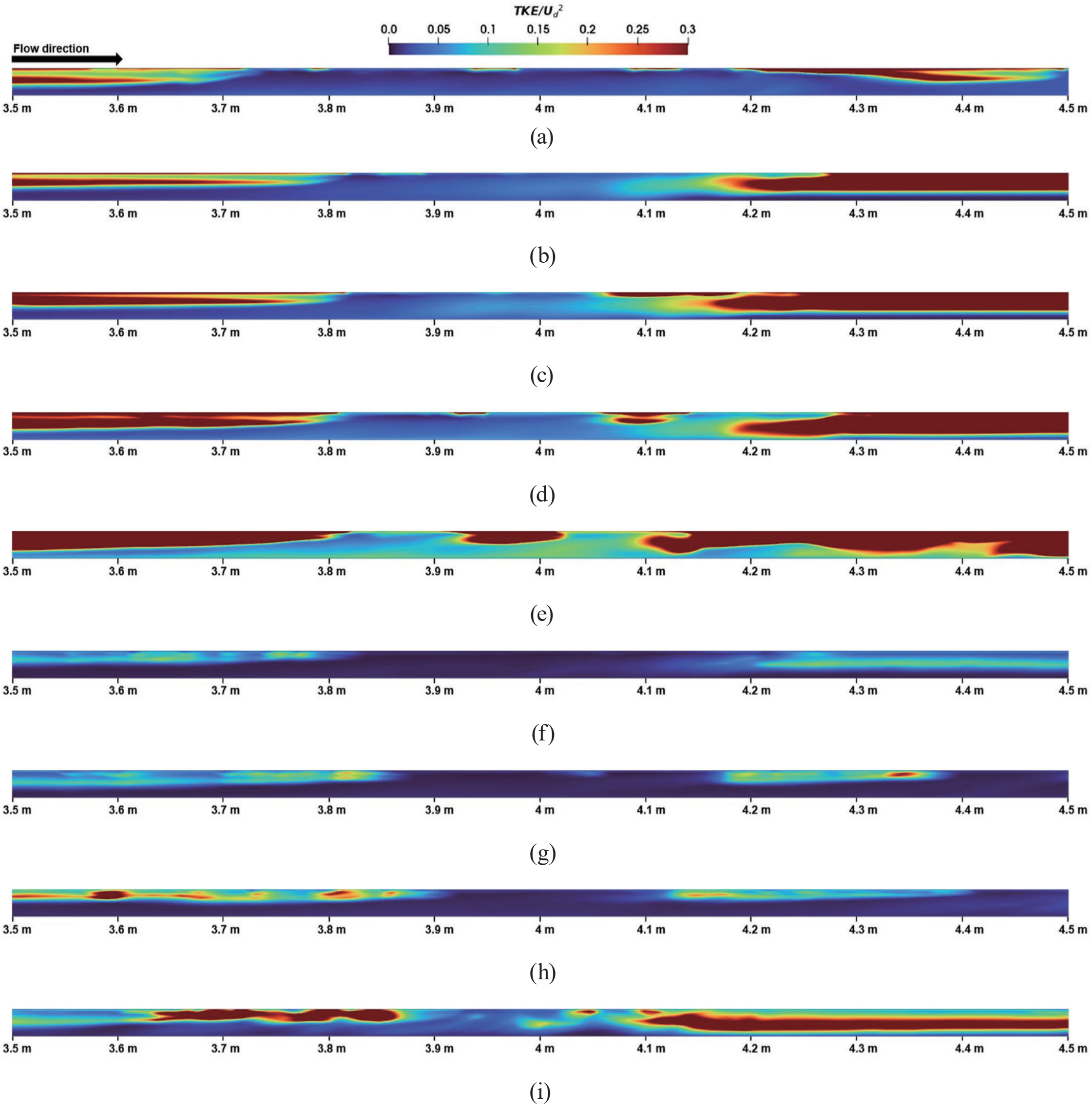

Fig. 9. (Color online) *TKE* contours at the center cross section. For Re_{SG} = 1377, Re_{SL} = 6500–16324: (a) Case 4, (b) Case 5, (c) Case 6, (d) Case 7, and (e) Case 8. For Re_{SG} = 4320, Re_{SL} = 2830–16500: (f) Case 9, (g) Case 10, (h) Case 11, and (i) Case 12.

distributed in the elongated bubble regions, with peak values concentrated along the liquid–gas interface. The *TKE* inside the liquid slug is low, forming values of TKE/U_d^2 below 0.05. Figure 9(b) shows that, at Re_{SL} = 7070, the region of TKE/U_d^2 above 0.3 gradually widens at the front and rear of the liquid slug, with a more pronounced increase at the front. In Fig. 9(c), at Re_{SL} = 9200, a trend similar to that of Re_{SL} = 7070 is observed for TKE/U_d^2. TKE/U_d^2 values above 0.3 appear over a wider range, and high *TKE* ratios are observed in the long air pockets inside the liquid slug. Figure 9(d) at Re_{SL} = 12730 shows that regions with TKE/U_d^2 above 0.3 form thickly at the slug front and rear, and values above 0.3 are also observed in some air pockets in the upper liquid slug region. In Fig. 9(e) at Re_{SL} = 16324, the region of TKE/U_d^2 above 0.3 expands, and notably, TKE/U_d^2 values of around 0.15 are confirmed to form inside the liquid slug. As shown in Fig. 9(f), under the $Re_{SG} = 4320$ condition with $Re_{SL} = 2830$, TKE/U_d^2 values of approximately 0.15 are observed at the liquid–gas interface. Figure 9(g) at $Re_{SL} = 7070$ shows TKE/U_d^2 values above 0.25 in some elongated bubble regions, but most remain around 0.1. In contrast, the *TKE* inside the liquid slug is low, reaching about $TKE/U_d^2 = 0.01$. In Fig. 9(h) at $Re_{SL} = 12730$, regions with TKE/U_d^2 above 0.3 begin to appear behind the slug, and elongated bubble regions with values above 0.2 are observed. The *TKE* ratio inside the liquid slug, however, remains low. In Fig. 9(i) at $Re_{SL} = 16500$, TKE/U_d^2 values of 0.05–0.1 appear inside the liquid slug, and high *TKE* ratios are observed at the liquid–gas interfaces at both the slug front and rear.

When $Re_{SG} = 1377$, high values of TKE/U_d^2, sometimes exceeding 2.0, are observed in the elongated bubble regions, while very low values below 0.15 are confirmed inside the liquid slug. The *TKE* ratio shows considerable differences primarily between the liquid and gas regions, with high values appearing mainly at the liquid–gas interface. These results indicate that the high *TKE* at the interface and in the elongated bubble regions is primarily due to the strong velocity gradients between the faster-moving gas and the slower liquid slug. The localized high *TKE* values near the interface suggest significant shear-induced turbulence, which can promote mixing and instabilities at the gas–liquid boundary. In addition, shear-layer-driven interfacial instabilities cause bubbles to be entrained at the front of the liquid slug.(25) The *TKE* distribution clearly indicates the presence of elevated *TKE* along the liquid–gas interfaces at both the front and rear of the liquid slug, and such localized increases are interpreted as major factors that enhance shear-layer instabilities and mixing. Accordingly, *TKE* serves as a critical parameter for characterizing slug behavior, suggesting that it can serve as a central metric for both quantitative and qualitative descriptions of slug flow structure in subsequent analyses.

4.4 Liquid volume

Figure 10 presents the time-averaged rate of liquid volume, V_L/V, under different superficial Reynolds number conditions. For each condition, the time-averaged values of V_L/V are shown together with the corresponding minimum and maximum values. The rate of liquid volume exhibits distinct trends depending on the gas Reynolds number Re_{SG}. Under the $Re_{SG} = 1377$ condition, V_L/V exhibits a progressive increase with Re_{SL} and remains relatively constant beyond $Re_{SL} = 12730$. In contrast, under the $Re_{SG} = 4320$ condition, V_L/V exhibits an almost linear increase with Re_{SL}. The comparion of the two conditions showed that V_L/V is higher for $Re_{SG} = 1377$ than for $Re_{SG} = 4320$ at the same Re_{SL}. The range between maximum and minimum V_L/V values is more pronounced at $Re_{SG} = 1377$, whereas it remains relatively consistent across the Re_{SL} range for $Re_{SG} = 4320$. The difference in the range of V_L/V reflects the intermittency, a characteristic feature of slug flow. The large variation in V_L/V under the $Re_{SG} = 1377$ condition indicates that liquid slugs and elongated bubbles appear alternately within a typical, well-separated liquid slug. In contrast, under the $Re_{SG} = 4320$ condition, the increased gas velocity causes substantial bubble entrainment within the slugs, resulting in a highly aerated slug flow pattern. In this process, the slugs fail to maintain a uniform and continuous form, leading to a significant reduction in V_L/V fluctuation range. These results suggest that the liquid volume

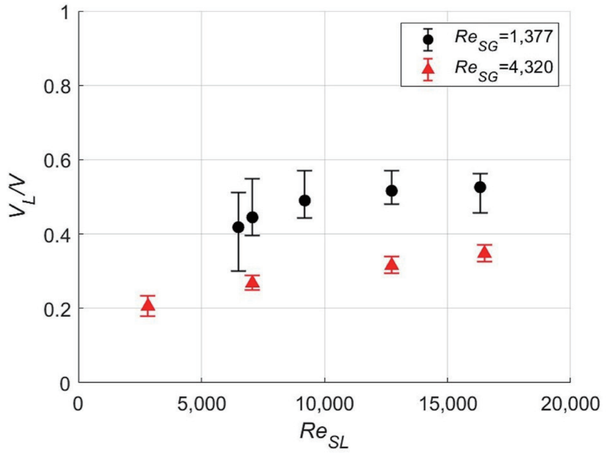

Fig. 10. (Color online) Rate of liquid volume for superficial Reynolds number.

fraction alone can capture certain aspects of slug flow characteristics; however, to precisely understand the overall slug period and distribution, a quantitative analysis of slug length, frequency, and flow distribution along the entire pipe will be necessary in future studies. Such additional analysis can more clearly clarify the correlation between liquid volume fraction and slug structure and serve as fundamental data for a deeper understanding of the governing factors of two-phase flow characteristics.

5. Conclusions

In this study, we conducted three-dimensional numerical simulations of liquid–gas two-phase flow using OpenFOAM to analyze slug flow characteristics. The characteristics of slug flow were examined, and hydraulic variables such as velocity and *TKE* were analyzed. The conclusions drawn are as follows.

1. Slug flow was characterized by alternating liquid slugs and elongated bubbles; this pattern was clearly observed under the Re_{SG} = 1377 condition. In contrast, under the Re_{SG} = 4320 condition, the bubble concentration within the liquid slug was high, and liquid droplet entrainment into the elongated bubble region was active at the rear of the slug. As ReSL increased, the liquid slug length decreased, the number of slugs formed along the pipe increased, and the elongated bubble region at the rear of the slug appeared narrower and longer than that at the front. This phenomenon was consistent with the results of previous hydraulic experiments, indicating that the 3D numerical model used in this study can reasonably reproduce the qualitative characteristics of two-phase slug flow.
2. The velocity distribution results under the Re_{SG} = 1377 condition showed that the velocity ratio U/U_m inside the liquid slug remained relatively low, at approximately 1.2, whereas a high velocity ratio of $U/U_m \geq 1.5$–2.0 appeared in the elongated bubble region. Under the Re_{SG} = 4320 condition, a high velocity ratio of $U/U_m \geq 2.0$ appeared in the elongated bubble region at both the slug front and rear due to the high gas velocity, while a relatively low velocity ratio of $U/U_m \approx 1.0$ occurred inside the liquid slug.

3. Under the Re_{SG} = 1377 condition, the *TKE* inside the liquid slug remained low, with $TKE/U_d^2 < 0.05$, while maximum values exceeding 2 were observed at the liquid–gas interface and in the elongated bubble regions. Under the ReSG = 4320 condition, high turbulence persisted, with $TKE/U_d^2 \geq 0.3$ at the slug front and rear liquid–gas interfaces, while the liquid slug maintained a low *TKE* ratio, approximately $TKE/U_d^2 \approx 0.01–0.1$. Consequently, *TKE* along the liquid–gas interface was found to increase owing to the strong shear generated by the relative velocity difference between the fast gas phase and the slower liquid slug.
4. The rate of liquid volume, V_L/V, exhibited different trends depending on the two gas Reynolds numbers. Under the Re_{SG} = 1377 condition, V_L/V gradually increased with Re_{SL} and remained relatively constant after Re_{SL} = 12730. In contrast, under the Re_{SG} = 4320 condition, V_L/V showed an almost linear increase with Re_{SL}. The comparison of the two conditions showed that V_L/V was higher for Re_{SG} = 1377 than for Re_{SG} = 4320 at the same Re_{SL}. Additionally, the maximum-minimum deviation was greater for Re_{SG} = 1377, while it remained relatively constant for Re_{SG} = 4320 across the entire Re_{SL} range. This phenomenon is considered to arise depending on whether liquid slugs and elongated bubbles intermittently alternate along the entire pipe, forming a clearly defined slug flow structure.

The present 3D numerical model has potential for application to two-phase flow analysis in underground stormwater tunnels. Further quantitative analysis of slug length and frequency along the entire pipe length is required to improve our understanding of slug flow characteristics. In addition, integrating numerical analysis with drone-based imaging data may help identify crack formation mechanisms and provide supporting guidance for concrete material selection in underground stormwater tunnels.

Acknowledgments

This work is financially supported by Korea Ministry of Climate, Energy, Environment (MCEE) as “Climate Resilient R&D Project for Water-Related Disaster Management) (RS-2024-00397821)”.

References

1 J. M. Mandhane, G. A. Gregory, and K. Aziz: Int. J. Multiphase Flow **1** (1974) 537. https://doi.org/10.1016/0301-9322(74)90006-8
2 Y. Taitel and A. E. Dukler: Int. J. Multiphase Flow **3** (1977) 585. https://doi.org/10.1016/0301-9322(77)90031-3
3 K. Kushiyama, S. Kamioka, and T. Yamada: J. Japan Soc. Hydrol. Water Resour. **16** (2003) 527.
4 E. Al Safran: J. Pet. Sci. Eng. **69** (2009) 143. https://doi.org/10.1016/j.petrol.2009.08.009
5 Q. Yang, Z. Ma, and S. Zhang: Water **14** (2022) 1. https://doi.org/10.3390/w14111760
6 P. Valluri, P. D. M. Spelt, C. J. Lawrence, and G. F. Hewitt: Int. J. Multiphase Flow **34** (2008) 206. https://doi.org/10.1016/j.ijmultiphaseflow.2007.09.001
7 C. Vallée, T. Höhne, H. Prasser, and T. Sühnel: Nucl. Eng. Des. **238** (2008) 637. https://doi.org/10.1016/j.nucengdes.2007.02.051
8 S. C. K. De Schepper, G. J. Heynderickx, and G. B. Marin: Chem. Eng. J. **138** (2008) 349. https://doi.org/10.1016/j.cej.2007.06.007
9 D. Lakehal, M. Labois, and C. Narayanan: Prog. Comput. Fluid Dyn. **12** (2012) 153. https://doi.org/10.1504/PCFD.2012.047458
10 M. Deendarlianto, M. Andrianto, A. Widyaparaga, O. Dinaryanto, Khasani, and Indarto: J. Pet. Sci. Eng. **147** (2016) 779. https://doi.org/10.1016/j.petrol.2016.09.019

11 J. López, H. Pineda, D. Bello, and N. Ratkovich: Exp. Therm Fluid Sci. **76** (2016) 126. https://doi.org/10.1016/j.expthermflusci.2016.02.013

12 M. Akhlaghi, V. Mohammadi, N. M. Nouri, M. Taherkhani, and M. Karimi: Chem. Eng. Res. Des. **152** (2019) 48. https://doi.org/10.1016/j.cherd.2019.09.031

13 OpenFOAM Foundation: OpenFOAM: The Open Source CFD Toolbox - User's Guide (OpenFOAM Foundation, London, 2024).

14 H. Weller: Report TR/HGW/04 (OpenCFD Ltd., 2008).

15 H. Adouni, Y. Chouari, W. Kriaa, and H. Bournot: Flow Meas. Instrum. **81** (2021) 1. https://doi.org/10.1016/j.flowmeasinst.2021.102013

16 S. L. Becker, C. N. M. Santos, C. F. Boos, H. H. Parno, V. Rossbach, H. F. Meier and M. K. Silva: Proc. 12th Spring School on Transition and Turbulence (ABCM, 2020) 46.

17 R. Vadrabade, R. S. Gulia, and J. Banerjee: Proc. 7th Int. and 45th National Conf. Fluid Mechanics and Fluid Power (IIT Bombay, 2018) 1–4.

18 J. Thaker and J. Banerjee: J. Pet. Sci. Eng. **135** (2015) 561. https://doi.org/10.1016/j.petrol.2015.10.018

19 O. J. Nydal, S. Pintus, and P. Andreussi: Int. J. Multiphase Flow **18** (1992) 439. https://doi.org/10.1016/0301-9322(92)90027-E

20 E. T. Hurlburt and T. J. Hanratty: Int. J. Multiphase Flow **28** (2002) 707. https://doi.org/10.1016/S0301-9322(02)00009-5

21 U. Kadri, R. F. Mudde, R. V. A. Oliemans, M. Bonizzi, and P. Andreussi: Int. J. Multiphase Flow **35** (2009) 1001. https://doi.org/10.1016/j.ijmultiphaseflow.2009.07.002

22 P. Y. Lin: Flow Regime Transitions in Horizontal Gas Liquid Flow (Doctoral dissertation, University of Illinois, Urbana, 1985) 77.

23 N. Andritsos, L. Williams, and T. J. Hanratty: Int. J. Multiphase Flow **15** (1989) 877. https://doi.org/10.1016/0301-9322(89)90017-7

24 J. Thaker and J. Banerjee: Int. J. Multiphase Flow **91** (2017) 63. https://doi.org/10.1016/j.ijmultiphaseflow.2017.01.014

25 E. Al-Safran, C. Kora, and C. Sarica: J. Pet. Sci. Eng. **133** (2015) 566. https://doi.org/10.1016/j.petrol.2015.06.032

About the Authors

Yongjun Kwon is currently pursuing his Ph.D. degree at Kunsan National University, Republic of Korea. His research interests include hydraulics engineering, computational fluid dynamics, and sediment transport modeling. (dydwns0507@kunsan.ac.kr)

Jae-Seon Yoon received his Ph.D. degree in Civil Engineering from Hanyang University, majoring in Water Resources and Coastal Engineering. He is currently conducting various numerical and hydraulic model studies at the Rural Research Institute of the Korea Rural Community Corporation. (jsun0757@ekr.or.kr)

Woochul Kang received his Ph.D. degree from Colorado State University, USA, in 2019. From 2019 to 2024, he was a Researcher at the Korea Institute of Civil Engineering and Building Technology (KICT). He is currently an Assistant Professor at Kongju National University. While his research interests cover a wide range of fields, his main area involves integrating water engineering—his primary major—with various technologies such as remote sensing and AI. (kang@kongju.ac.kr)

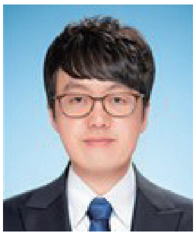

Hyung-Suk Kim received his Ph.D. degree in Civil Engineering from Hokkaido University, Japan. He served as a junior and senior researcher at the Korea Institute of Civil Engineering and Building Technology (KICT). Since 2020, he has been an assistant professor in the Department of Civil Engineering at Kunsan National University, Republic of Korea. His research interests include hydraulics and coastal engineering, sediment transport and morphodynamics, scouring, and the ecological modeling of fish populations. (hskim0824@kunsan.ac.kr)